Glioblastoma Detection with Hyperspectral Image Analysis through Optimal Wavelength Selection

Citation for published version (APA):
Verbers, M., Manni, F., Fabelo, H., Leon, R., Burström, G., Lagares, A., Piñeiro, J. F., Morera Molina, J., Marrero Callicó , G., & Zinger, S. (2025). Glioblastoma Detection with Hyperspectral Image Analysis through Optimal Wavelength Selection. In *2025 47th Annual International Conference of the IEEE Engineering in Medicine and Biology Society, EMBC 2025* Article 11252746 Institute of Electrical and Electronics Engineers. https://doi.org/10.1109/EMBC58623.2025.11252746

Document license:
CC BY

DOI:
10.1109/EMBC58623.2025.11252746

Document status and date:
Published: 03/12/2025

Document Version:
Publisher’s PDF, also known as Version of Record (includes final page, issue and volume numbers)

Please check the document version of this publication:

• A submitted manuscript is the version of the article upon submission and before peer-review. There can be important differences between the submitted version and the official published version of record. People interested in the research are advised to contact the author for the final version of the publication, or visit the DOI to the publisher's website.
• The final author version and the galley proof are versions of the publication after peer review.
• The final published version features the final layout of the paper including the volume, issue and page numbers.

Link to publication

General rights
Copyright and moral rights for the publications made accessible in the public portal are retained by the authors and/or other copyright owners and it is a condition of accessing publications that users recognise and abide by the legal requirements associated with these rights.

- Users may download and print one copy of any publication from the public portal for the purpose of private study or research.
- You may not further distribute the material or use it for any profit-making activity or commercial gain
- You may freely distribute the URL identifying the publication in the public portal.

If the publication is distributed under the terms of Article 25fa of the Dutch Copyright Act, indicated by the “Taverne” license above, please follow below link for the End User Agreement:

www.tue.nl/taverne

Take down policy
If you believe that this document breaches copyright please contact us at:

openaccess@tue.nl

providing details and we will investigate your claim.

Download date: 08. abr. 2026

2025 47th Annual International Conference of the IEEE Engineering in Medicine and Biology Society (EMBC) | 979-8-3315-8618-8/25/$31.00 ©2025 Authors | DOI: 10.1109/EMBC58623.2025.11252746

Glioblastoma Detection with Hyperspectral Image Analysis through Optimal Wavelength Selection

Max Verbers[1,*], Francesca Manni[1], Himar Fabelo[2,3,4], Raquel Leon[4], Gustav Liu Burström[5], Alfonso Lagares[6], Juan F. Piñeiro[2], Jesus Morera Molina[2], Gustavo M. Callico[4], Svitlana Zinger[1]

Abstract— **Glioblastoma is the most aggressive and common type of malignant primary brain tumor. Neurosurgery is one of the main treatments for the removal of glioblastoma tumors. Although complete tumor resection is crucial, excessive removal of brain tissue can cause unwanted impairment. Intraoperative techniques for tumor detection and delineation can help to achieve a more precise resection and improve the clinical workflow and outcomes. This study explores the use of hyperspectral imaging for detecting glioblastoma during surgery. To this end, a database of 24 images from 14 patients is studied by employing an image analysis framework, which entails spectral and spatial dimensionality reduction and classification. Multiple AI-based methods are presented and tested for the detection of healthy tissue and glioblastoma, as well as techniques for reducing HSI dimensionality, thereby facilitating the clinical applicability of HSI. A multi-layer perceptron shows the highest macro F1 score of 86.65%, when 20 hyperspectral wavelengths are automatically selected by using the Ant Colony optimizer. The proposed approach outperforms the state-of-the-art methods, which use datasets including multiple grades and solely grade 4 tumors. The results demonstrate that HSI combined with a proper image analysis framework, aiming at reducing spectral and spatial dimension, has the potential to aid tumor detection during brain surgery.**

Clinical Relevance— **This paper demonstrates the feasibility of grade 4 brain tumor detection with hyperspectral image analysis using a set of most informative spectral wavelengths, outperforming the state-of-the-art approaches and paving the way for further advancements and applications of non-invasive imaging techniques to improve image-guided glioblastoma surgery.**

I. INTRODUCTION

Brain and nervous system cancer was the 12th most common cause of cancer mortality in 2022, with an estimated 321,000 cases and 248,000 deaths reported globally [1]. The standard treatment protocol for malignant brain tumors includes a combination of neurosurgery, radiotherapy, and chemotherapy. Maximizing the extent of resection can reduce mortality rates, recurrence, and potential complications and side effects in patients [2]–[5]. In contrast, excessive resection can cause permanent neurological impairment; however, immediate damage is counterbalanced by long-term benefits [6]. Therefore, achieving a precise resection during neurosurgery can significantly improve postoperative patient outcomes and care.

Brain tumors, particularly gliomas, tend to diffusely infiltrate surrounding brain tissue, making it difficult for surgeons to distinguish between normal and tumor tissue, even with microscopic guidance [7]. Currently, surgical procedures are guided by pre-operative imaging techniques such as Magnetic Resonance Imaging (MRI) and Computed Tomography (CT), used in conjunction with neuronavigation systems [8]. However, these methods have several limitations, such as brain shift, lengthy scanning procedures, and lack of real-time feedback. Brain shift is a significant challenge due to the alteration of the boundaries of brain tumors during surgery [9]. This dynamic change complicates the process of accurately delineating the tumor.

Advances have been made to improve intraoperative procedures. Intraoperative MRI (iMRI) addresses brain shift, but prolongs surgery and procedure time and introduces challenges related to patient safety, monitoring, and special equipment requirements [10], [11]. Recently, intraoperative Ultrasound (iUS) has gained attention for its faster acquisition time compared to iMRI [12]. However, challenges remain in the registration of 2D iUS images in a 3D volume, and artifacts can occur when the resection cavity is filled with fluids, misleading the clinical interpretation [13]. In addition, intraoperative fluorescence agents such as 5-aminolevulimic acid or fluorescein sodium are common for intraoperative tumor delineation. Nevertheless, results vary due to differences in agents, the amount administered, timing, and location of biopsy samples taken during surgery [14]. For these agents, it is challenging to identify infiltrative tumor cells, leading to false positives in normal brain tissue and potentially excessive or inadequate tissue removal [15]. In particular, the differentiation of low-grade gliomas with fluorescence agents is more difficult than high-grade gliomas.

The gap in effective intraoperative delineation of brain tumors can be addressed by applying novel optical imaging techniques such as Hyperspectral Imaging (HSI) [16]–[21]. HSI enables to see beyond the human perception and it has the advantages of being non-contact, label-free, and non-ionizing. In recent years, research on HSI has advanced significantly [21]–[23]. Studies show promising results in fields such as medical tissue analysis [24], remote sens-

---

* `m.verbers@tue.nl`

[1] Dept. of Electrical Engineering, Eindhoven University of Technology, Eindhoven, The Netherlands

[2] Fundacion Canaria Instituto de Investigacion Sanitaria de Canarias (FIISC), Las Palmas de Gran Canaria, Spain

[3] Research Unit, Hospital Universitario de Gran Canaria Dr. Negrin, Las Palmas de Gran Canaria, Spain

[4] Institute for Applied Microelectronics (IUMA), Universidad de Las Palmas de Gran Canaria, Las Palmas de Gran Canaria, Spain

[5] Dept. of Neurosurgery, Karolinska University Hospital, Stockholm, Sweden

[6] Dept. of Neurosurgery, Hospital Universitario 12 Octubre, Dept. of Surgery, Medicine Faculty, Universidad Complutense de Madrid, Instituto de Investigaciones Sanitarias (imas12), Madrid, Spain

ing [25], agriculture [26], [27], food safety [28], forensics [29], [30], and military [31]. Despite this progress, more studies are needed with larger datasets to facilitate HSI in clinical adoption. The spatial and spectral capabilities of HSI allow for the exploitation of structural and biochemical differences between normal and cancer cells, aiding in cancer detection. This has led to the first establishment in neurosurgical HSI [32]–[34], stimulating data acquisition and further development in the field.

Hyperspectral (HS) images can be used to classify brain tumors by applying an appropriate framework for preprocessing, band selection, and classification. The preprocessing stage involves HS image normalization and calibration with respect to the dark and white reference images. Band selection varies according to the specific study objectives, where the main objective of this step is fewer wavelengths. A high number of wavelengths increases the size of the HS data, prolongs processing times, complicates data interpretation, and introduces redundancy information, which can lead to misclassification. Ultimately, when the most informative wavelengths have been found, the redundant wavelengths can be ignored when capturing new HS images. HS image classification aims at discriminating different types of brain tissue, with models including Support Vector Machines (SVMs) [18], [19], Convolutional Neural Networks (CNNs) [17], [35], and Deep Neural Networks (DNNs) [20], [21]. Recent advances in the remote sensing field have also introduced novel algorithms such as transformers and CNNs, [36]–[40], which can beneficial for this study.

This study presents novel approaches in HSI wavelength reduction, spatial patching, and explores multi-class classification techniques towards a clinical application of HSI in the surgical scenario. In particular, we propose advancements in HSI wavelength selection and demonstrate substantial improvements over recent studies, selecting a low number of wavelengths that facilitate faster processing time for intraoperative HSI solutions. Additionally, we explore the impact of spatially patching pixels within HS brain images to assess its influence and potential advantages in the HS image analysis. Furthermore, both conventional and novel classification algorithms, such as SVMs, Random Forests (RF), Hybrid Spectral Net (HybridSN), and Spectral-Spatial Feature Tokenization Transformer (SSFTT) are explored. This work differentiates itself from current state-of-the-art research by using a larger glioblastoma dataset to demonstrate its findings, with a focus on re-evaluating, enhancing, and comparing with state-of-the-art wavelength reduction algorithms. The final classification results are benchmarked for accuracies and presented in classification maps with the aim of facilitating the application of HSI in clinical practice. Overall, this study proposes an accurate grade 4 tumor delineation for neurosurgeons, ultimately improving patient care and surgical outcomes.

II. METHODS

This section provides a description of the proposed method. An overview of the studied approach is shown in Figure 1 and entails: data calibration and normalization, wavelength reduction, spatial patching, and image classification for brain tumor detection. For the latter three steps, multiple methods are separately analyzed.

A. Hyperspectral Image Data

A publicly available intraoperative HS database consisting of 61 images from 34 adult patients was employed [21]. These images were captured at the University Hospital of Gran Canaria Doctor Negrín (Spain) using a VNIR HS push-broom camera (Hyperspec® VNIR A-Series, Headwall Photonics Inc., Fitchburg, MA, USA). The HSI camera captures 826 spectral channels in the 400 to 1000 nm range. The maximum spatial resolution of the dataset is 741×1004 pixels. In this study, 24 images of 14 patients with histopathologically confirmed grade 4 glioblastoma (GB) are analyzed. An example of an image used in this study is shown in Figure 2.

B. Calibration and Normalization

Preprocessing of HSI data significantly enhances image analysis for classification purposes, since HS data generally exhibit system artifacts caused by environmental factors [41]. To address this, two preprocessing steps are employed: HS calibration and pixel-by-pixel normalization. For calibration the raw reflectance data (I_{raw}), a white reference image (I_{white}), and a dark reference image (I_{dark}), are used to calculate the calibrated corrected image (I_c) as follows:

$$I_c = \frac{I_{raw} - I_{dark}}{I_{white} - I_{dark}} \tag{1}$$

The dark and white references are obtained by keeping the camera shutter closed and using a white diffuse reflectance target, respectively. Normalization involves homogenizing the reflectance levels, pixel by pixel, between 0 and 1 via the following equation:

$$P_{i,norm} = \frac{P_i - P_{min}}{P_{max} - P_{min}} \tag{2}$$

Here, P_i is the reflectance value of the wavelength i, P_{min} and P_{max} are the lowest and highest reflectance levels, respectively, considering every wavelength, and $P_{i,norm}$ is the normalized value.

C. Wavelength Selection

To improve the processing efficiency while retaining performance and eliminating redundant information, spectral band reduction is performed. Spectral channels above 909 nm are removed due to noisy acquisition circumstances, as suggested in recent research [42].

In this study, three different reduction methods are employed: (1) a conventional method used via band averaging [42], (2) the Recursive Feature Elimination (RFE) method [43], and (3) the Ant Colony Optimization (ACO) method [44]. Band averaging involves selecting bands based on a wavelength interval larger than the original HS data, with a sampling interval of 3.61 nm between 440 and 909 nm, results in 128 bands. RFE uses a recursive algorithm

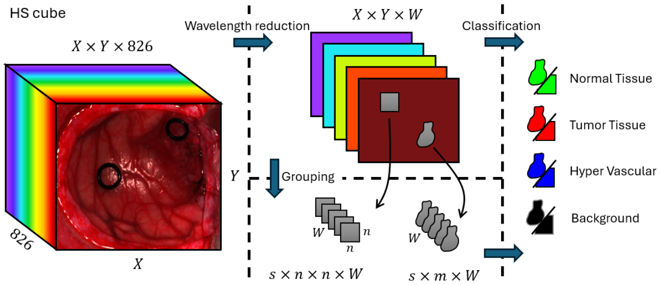

Fig. 1. Proposed framework. The HS cube is preprocessed resulting in an $X \times Y \times 826$ cube. X and Y are the horizontal and vertical spatial dimensions with 826 wavelengths. Wavelength reduction is performed on the preprocessed HS cube, where the 826 wavelengths are reduced to a chosen number W. Optionally patching can be applied to create a grid in the data of $n \times n$ equal non-overlapping blocks. s represents the number of samples, i.e. the number of blocks the image can be split into. Finally, either per pixel or per patch, classification can be performed.

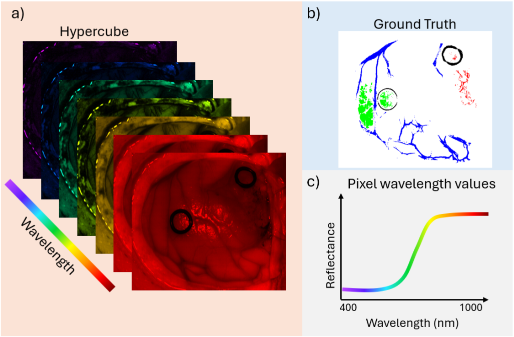

Fig. 2. Example of a HS cube from the intraoperative brain dataset. **a)** An illustration of the data cube. **b)** The ground truth where green is normal tissue, red is tumor tissue, blue is blood vessel and black is background. **c)** An example graph showing a single pixel's reflectance values across the HS wavelength range.

TABLE I

NUMBER OF PIXELS FOR THE TRAINING AND TEST DATA PER CLASS

Class	Normal Tissue	Tumor Tissue	Blood Vessels	Background
Training	67,320	11,350	38,590	95,308
Test	75,871	4,884	14,506	36,416

to eliminate the least informative wavelengths. It evaluates performance across all wavelengths using cross-validation and iteratively removes the least informative wavelengths until a predefined lower bound of features is reached. The optimal number of wavelengths is then selected based on the highest calculated performance. The ACO method, inspired by the behavior of ants finding the shortest path to food, is a genetic algorithm aimed at identifying the optimal combination of a specified number of wavelengths from the entire set [17]. In the ACO algorithm, ants leave pheromones on paths with higher performance. Each path represents a single wavelength, and the goal is to find the combination of wavelengths with the highest performance. Initially, all wavelengths start with the same number of pheromones, and an ant will start at each wavelength. The probability of an ant moving from the current wavelength to another wavelength is:

$$p_{wc} = \frac{\tau_{wc}}{\sum_w \tau_{wa}} \ \forall \ w \in allowed_w \tag{3}$$

Here, p_{wc} is the probability of moving to a certain wavelength w, τ_{wc} are the pheromones on the current wavelength, and $allowed_w$ are the wavelengths that have not yet been selected by this ant. τ_{wa} are all wavelengths allowed. Once all ants have selected n number of wavelengths, the pheromones are updated based on the equation:

$$\tau_w = \rho \tau_w + \Delta\tau_w \tag{4}$$

where ρ is the dissipation factor of the pheromone and $\Delta\tau_w$ represents the pheromones left by all the ants. The number of pheromones left per ant is:

$$\Delta\tau_w = \begin{cases} Q \cdot score & \text{if } w \text{ is selected by an ant} \\ 0 & \text{otherwise} \end{cases} \tag{5}$$

where Q is a constant that adjust the pheromone range, $score$ is the average macro F1 score of 5-folds on the selected wavelengths employing a linear SVM. When all pheromones have been updated, a new generation of ants can find their paths with a higher likelihood of walking over wavelengths that score high. After several iterations, the wavelengths that resulted in the highest F1 score across all classes are selected.

D. Spatial Patching Techniques

In this study, an approach for HS spatial patching is explored to introduce a spatial relationship among pixels during HS image classification, which is lacking when a pixel-wise based approach is used. Each HS cube can be represented as an image sized $X \times Y \times W$, where X is the height, Y the width, and W the number of captured wavelengths. Spatial patching enables noise reduction and better generalization in the classification step [45]. For patching, the image is divided into $n \times n \times W$ patches, with zero-padding to ensure that $\frac{X}{n}$ and $\frac{Y}{n}$ are integers, adapting the labeled pixels accordingly. In this study, patches of 1x1, 6x6, 11x11, and 22x22 are explored and compared.

E. Classification

The goal of the classification step is to distinguish between cancerous pixels and non-cancerous pixels. Machine learning and deep learning algorithms are exploited, including linear SVMs, Radial Basis Function (RBF) SVMs, RF, Multilayer Perceptron (MLP), HybridSN [36], and SSFTT [38].

F. Performance Evaluation

The complete dataset is randomly divided patient-wise into training and test sets, with a split of 70% - 30%, respectively, based on the number of tumor pixels, as shown in Table I. The test set is used for the final evaluation of each experiment. To evaluate, all algorithms for wavelength reduction are trained and classified using a 5-fold cross-validation and a linear SVM, while classification training is performed with leave-one-patient-out cross-validation (LOPOCV). The primary classification metric used in this study is the F1 score, which provides a balanced measure of performance and is defined as:

$$\text{F1 score} = \frac{2TP}{2TP + FP + FN}, \tag{6}$$

TABLE II

TEST RESULTS FOR HSI WAVELENGTH SELECTION

Number of Wavelengths	RFE Macro F1 score	RFE Tumor Precision	RFE Tumor Recall	ACO-P Macro F1 score	ACO-P Tumor Precision	ACO-P Tumor Recall	ACO-G Macro F1 score	ACO-G Tumor Precision	ACO-G Tumor Recall
5	65.22%	65.02%	5.67%	56.67%	0%	0%	64.76%	100%	0.13%
10	77.04%	74.95%	23.65%	59.04%	0%	0%	79.22%	88.29%	37.74%
20	76.11%	77.74%	20.17%	78.78%	83.33%	28.19%	**85.68%**	84.87%	59.05%
50	74.63%	83.36%	11.69%	83.77%	78.20%	34.30%	84.20%	87.50%	49.42%
100	**83.04%**	78.90%	33.54%	**86.83%**	80.57%	44.92%	82.06%	81.92%	47.11%

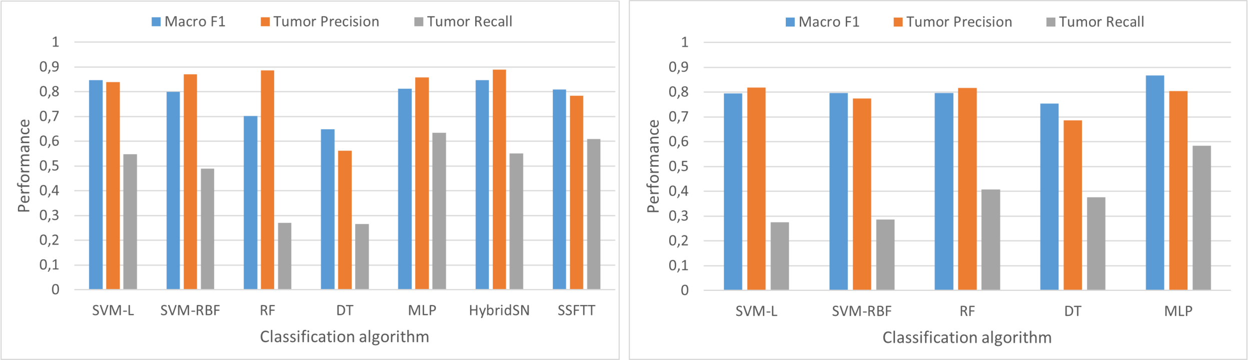

(a) Patch-wise results (b) Pixel-wise results

Fig. 3. Final classification results for tumor detection by employing different classifiers (a) Patching-based classification results and (b) pixel-wise classification results. In the barplot, *Blue* represents the Macro F1 score over the four classes, *Orange* the tumor precision, and *Grey* the tumor recall.

TABLE III

PATCH-BASED PERFORMANCES FOR DIFFERENT WINDOW SIZES

Window size	1x1	6x6	11x11	22x22
F1-Normal tissue	**95.22%**	94.96%	84.67%	74.27%
F1-Tumor tissue	42.13%	**69.64%**	47.30%	21.25%
F1-Blood vessels	**90.49%**	84.57%	69.76%	51.25%
F1-Background	87.28%	**93.53%**	89.48%	76.35%
F1-Macro average	78.78%	**85.68%**	72.80%	55.78%

where TP are the true positives, FP the false positives, and FN the false negatives.

A qualitative assessment of the algorithm is done through extensive exploration of multiple parts of the framework and also replicating related studied algorithms on wavelength reduction. The experiments can be divided into two parts. First, wavelength selection experiments are performed to find the most optimal subset of HS wavelengths. Selected wavelengths are tested using a linear SVM. The SVM is computationally inexpensive and employed in related studies [17], [44], both of which help to prove the feasibility of the study. Second, once optimal wavelengths are identified, experiments that focus on finding the best classification algorithm are explored. In these steps, the influence of spatial patching on the final classification result is studied.

III. RESULTS

In this section, four experiments are described. Each experiment and its results will be used in subsequent experiments. The first two experiments are designed to 1) find the optimal set of wavelengths and 2) evaluate the impact of spatial dimensionality reduction on the final classification outcome. These experiments evaluate the number of wavelengths and the size of a single patch for the patching algorithm. The third experiment focuses on evaluating different classification algorithms, which are conventional algorithms, already evaluated by Fabelo *et al.* on a smaller datasets [46], and studying their performance. The fourth experiment benchmarks the selected wavelengths against other wavelength-selection methods.

A. Wavelength Selection Performances

The RFE and ACO retrieve 5, 10, 20, 50, and 100 wavelengths. Both algorithms employ a linear SVM with a 5-fold cross-validation to update every iteration. The hyperparameter of the SVM, C, is empirically chosen to be 1 for RFE and 20 for ACO. The final result is tested on unseen data. The RFE algorithm is evaluated using a pixel-wise strategy, whereas the ACO is evaluated using the pixel (ACO-P) and patching 6x6 (ACO-G) strategy. These results are shown in Table II.

The results show that both RFE and ACO-P achieve performance similar to those obtained by the band averaging. As a benchmark, the band averaging algorithm with 128 wavelengths [42] is re-evaluated, employing pixel-wise, with a linear SVM on the same dataset, which achieves a Macro F1 score of 88.7%, a tumor precision of 83.26%, and a tumor recall of 53.05%. However, when wavelength selection algorithms choose fewer wavelengths, they are prone to overfitting, particularly resulting in poor recall for the tumor class. There is also a slight increase in performance when comparing the ACO-P and ACO-G results, where a clear increase is visible between selecting 10 or 20 wavelengths. The 20 wavelengths found in the ACO-G achieve a performance almost similar to that of band averaging (128 wavelengths), outperforming tumor recall with 5%. The 20 wavelengths found with the ACO-G are: 466.7, 543.8, 548.2, 556.2, 588.2, 604.9, 623.8, 640.6, 642.8, 702.4, 723.5, 739.5, 748.3, 749.7, 759.2, 818.1, 823.2, 830.5, 866.9, and 912.0 nm.

B. *Influence of Patching in Wavelength Selection*

The 20 wavelengths previously found by the ACO-G algorithm are used to study the impact of patching in wavelength selection. The window sizes tested are 1x1, which means that patching has not been applied, 6x6, 11x11, and 22x22. Similarly to the wavelength selection performances, the algorithm is 5-fold cross-validated and tested on unseen data. The results of the patching performance can be found in Table III. The 6x6 window size achieves higher overall performance, with the main difference shown in the tumor tissue class. When the window size increases, the performances drop, with the greatest impact in the most under-represented classes, i.e., tumor tissue and blood vessels.

C. *Performance of Classifiers*

The best 20 wavelengths found by the ACO-G are selected and used in both patching and pixel-based classification methods. The optimization parameters are the following. SVM-L cost is 2^6 and 2^2 for SVM-RBF which has a gamma of 2^{-6}. The maximum depth of the decision tree is 30 while the number of trees selected for the RF is equal to 50. The MLP contains 100 neurons and a learning rate of 0.01 is used for training purposes (the same value is selected for SSFTT). These hyperparameters of the best-performing algorithms are evaluated with the test set. The HybridSN model that achieves higher classification performance has three 3D convolutional layers, one 2D convolutional layer, and three dense layers, the last being a softmax layer. In Figure 3(a) the results of the classification that includes 6x6 patching are illustrated, and Figure 3(b) depicts the results without patching.

The best overall performing algorithm is the pixel-wise MLP with a macro F1 score of 86.65%, followed by the HybridSN and the SVM-L patching variant with macro F1 scores of 84.72% and 84.67%, respectively. The RF and DT algorithms have the lowest performance. An overall trend across the classification algorithms is that when patching is applied, the tumor class is detected with higher accuracy. However, the other classes are slightly underperforming compared to the pixel-wise approach, especially the blood vessel class which has a reduction of 10% in its F1 score. Figure 4 shows the qualitative result of the classification of two patients from unseen data using the processing framework based on the ACO algorithm (20 wavelengths) and the pixel-wise MLP algorithm for classification purposes. In the classification map, normal tissue, tumor tissue, blood vessels, and background are represented in green, red, blue, and black, respectively.

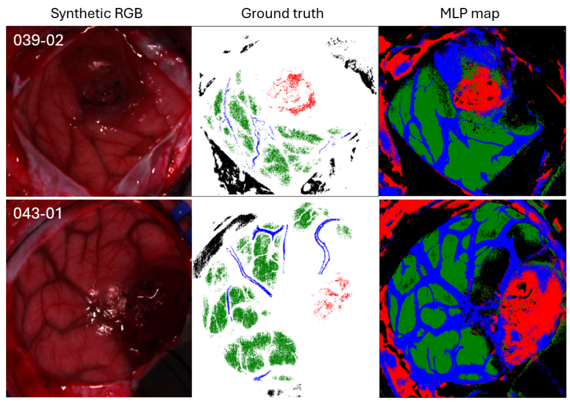

Fig. 4. An example of the original synthetic RGB, the ground truth and the classification map when the pixel-wise MLP classifier is applied with 20 wavelengths of ACO-G. Images of patients 39 and 43 are depicted. Normal tissue, tumor tissue, blood vessels and background are represented in green, red, blue and black, respectively. White pixels in the ground truth represent non-labeled pixels.

TABLE IV

BENCHMARK MACRO F1 SCORE PERFORMANCE OF 4 DIFFERENT WAVELENGTH SETS

Algorithm	# Wavelengths	MLP	HybridSN	SVM-L
1) Set [17]	100	84.45%	83.69%	70.23%
2) Set adapted [17]	100	**87.37%**	84.12%	**85.58%**
3) Averaging [42]	128	86.48%	**89.08%**	84.35%
4) Proposed	20	86.65%	84.72%	84.67%

D. *Comparison of the Wavelength Partitions with the State-Of-The-Art Selections*

In order to have a quantitative comparison, Table IV shows four wavelength selections, where the algorithms with the best performances analyzed in this study are compared against selected wavelength sets from other studies. The sets are 1) from previous related work by Manni *et al.* [17], 2) the method proposed in 1) and applied for the dataset analyzed in this study, 3) the wavelength average used in [20], [21], [42], and 4) our 20 proposed wavelengths. The results show that the performance is similar in the top 3 performing algorithms, i.e., MLP, HybridSN and the SVM-L. Both MLP and HybridSN have very high consistent F1 scores, between 84% and 89%. The main difference in performance is between classes, where HybridSN scores 9% higher in the tumor class and 10% lower in the blood vessel class compared to the MLP algorithm. The SVM-L of set 1) is the only odd score, which can be related to a poor tumor F1 score of 19%, likely due to few data points and overfitting as a consequence. Overall, SVM-L achieves lower accuracy compared to the MLP and HybridSN algorithms.

IV. DISCUSSION

Effective treatment of brain tumors remains a significant challenge, driving the need for novel, non-ionizing, contact-free methods that enable precise tumor detection and delineation. HSI has shown considerable potential to address this challenge and its feasibility has been demonstrated in previous works [16], [18], [21]. In this study, a dataset of grade 4 brain tumors was used to design and test a framework that exploits both spatial and spectral information in the HS data aiming at improving the detection of tumor, normal tissues, and blood vessels during surgery.

In this framework, the most informative wavelengths are selected using the RFE and ACO algorithms, considering the possible influence of patching. Patching enhances the information needed for classification algorithms to relate spatial structures to labeled classes, improving overall performance. The RFE algorithm has been found to be less effective in identifying suitable wavelengths. Since the algorithm removes wavelengths in every iteration, in initial iterations it can lead to removal of informative wavelengths where the tumor is captured due to their under-representation. This causes an improvement for wavelengths that retain non-tumor tissue, thereby eliminating those wavelengths that are crucial for tumor classification, as shown in Table II. Instead, the ACO algorithm includes all wavelengths in each iteration, increasing the probability of selecting informative wavelengths at lower number of wavelengths. In this study a linear SVM is applied to optimize the wavelength selection. However, in future work, a deep learning model can be exploited to select HS wavelengths. Four of the seven wavelengths selected by a previous study [19] are within a 10 nm range of the wavelengths proposed in this study, and six of the eight wavelength ranges detected by [17] overlap with the wavelengths proposed.

Another important aspect is the influence of image patching in the HSI wavelength selection. This study shows that when the patching window size increases, the algorithms generalize less, see Table III. This means that when a patching area is large (e.g. 11x11 and 22x22 pixels) and covers different tissue types, the classification performances decrease. In particular, image areas representing blood vessels are more sensitive to larger window sizes, likely due to their smaller size. When observing the chosen wavelengths per window size, the 1x1 window emphasizes the wavelength range of 436-469 nm and 830-945 nm. The 6x6 configuration is more represented in the 540-640 nm and 700-760 nm wavelength ranges. For the 11x11 window size, there is a higher representation of the wavelength range between 500-530 nm and 580-618 nm. Lastly, the 22x22 window represents the most widespread coverage across all wavelengths. Although alternative approaches for spatial feature selection can be considered, in this feasibility study we focused on evaluating the impact of image patching to limit the processing time in the entire image analysis frameworks, towards an application in the clinical scenario.

Overall, the classification results (in particular precision and recall for tumor detection) demonstrate that patching has a positive impact on the tumor detection outcome of the designed framework. However, the pixel-wise MLP variant outperforms all other classification methods for the non-tumor class classification. Another observation is that algorithms based on neural networks (MLP, HybridSN, and SSFTT) outperform conventional machine learning algorithms, such as SVM and ensemble-based methods, in tumor detection.

TABLE V

COMPARISON AGAINST STATE-OF-THE-ART

Approach	# Pts	# Ims	Grade	# WL	Macro F1-score	Overall Accuracy
SVM [19]	16	26	1-4	7		73%
SVM [18]	12	13	3,4	25		60%
CNN [17]	9	12	4	100		80%
DNN [21]	34	61	1-4	128	70.2%	87%
DNN [20]	16	26	1-4	128		80%
Proposed	14	24	4	20	**86.65%**	**93%**

Number of patients (# Pts), images (# Ims), and wavelengths (# WL)

Table V includes related works that implement algorithms for different numbers of patients, grades of brain tumors, and number of wavelengths. This shows the added value of focusing exclusively on grade 4 tumors, as this selection leads to improved performance in tumor delineation, thus mitigating biases. However, extensive datasets including different grades should be studied to improve the performance of such models across different tumor stages. Figure 4 shows the classification map of patient no. 39 and no. 43. In the non-brain area (image borders), clear misclassification of background pixels occurs. Similarly in the parenchyma, brain tissue (e.g., normal or tumor tissue) is classified as the background. This may be caused by poor lighting conditions which can be improved by adopting a standardized and optimized image acquisition protocol among patients.

The consistency of high-scoring algorithms - MLP, HybridSN, and SVM-L - confirms that limited spectral wavelengths are sufficient to identify tumors, also mentioned in recent studies [19].

V. CONCLUSIONS

This study demonstrates that intraoperative grade IV brain tumor delineation combined with a proper HSI-based image analysis framework enables the differentiation of malignant and normal tissue and blood vessels. Advancements in wavelength selection are proposed and combined with spatial feature reduction in the HSI data, leading to better classification outcomes. The MLP algorithm, combined with the 20 wavelengths found by the ACO-G algorithm, achieves on average an F1 score of 86.65%. The wavelength selection reduces the data complexity, thus decreasing the overall processing time, which is crucial during glioblastoma surgery.

Moreover, glioblastoma tumor classification is extensively studied by applying and benchmarking machine learning and deep learning-based techniques, thereby paving the way for facilitating the application of HSI in clinical practice. Future work may explore different methods for spatial dimensionality reduction, with larger datasets including a variety of glioma grades.

VI. ACKNOWLEDGMENT

This work has been developed under the STRATUM project which received funding from the European Union's Horizon Europe Programme HORIZON-IA action under grant agreement No 101137416.

REFERENCES

[1] F. Bray, M. Laversanne, et al., "Global cancer statistics 2022: GLOBOCAN estimates of incidence and mortality worldwide for 36 cancers in 185 countries," *CA: a cancer journal for clinicians*, vol. 74, no. 3, pp. 229–263, 2024.

[2] M. Lacroix, D. Abi-Said, et al., "A multivariate analysis of 416 patients with glioblastoma multiforme: prognosis, extent of resection, and survival," *Journal of Neurosurgery*, vol. 95, pp. 190–198, 2001.

[3] M. J. McGirt, K. L. Chaichana, et al., "Extent of surgical resection is independently associated with survival in patients with hemispheric infiltrating low-grade gliomas," *Neurosurgery*, vol. 63, pp. 700–707, 2008.

[4] J. S. Smith, S. M. Chang, et al., "Role of extent of resection in the long-term outcome of low-grade hemispheric gliomas," *Journal of Clinical Oncology*, vol. 26, pp. 1338–1345, 2008.

[5] N. Sanai, M. Y. Polley, et al., "An extent of resection threshold for newly diagnosed glioblastomas: Clinical article," *Journal of Neurosurgery*, vol. 115, pp. 3–8, 2011.

[6] W. Stummer, J. C. Tonn, et al., "Counterbalancing risks and gains from extended resections in malignant glioma surgery: a supplemental analysis from the randomized 5-aminolevulinic acid glioma resection study: Clinical article," *Journal of Neurosurgery*, vol. 114, pp. 613–623, 2011.

[7] F. Seker-Polat, N. P. Degirmenci, et al., "Tumor cell infiltration into the brain in glioblastoma: From mechanisms to clinical perspectives," *Cancers*, vol. 14, 2022.

[8] D. C. Birkhoff, A. S. H. M. van Dalen, and M. P. Schijven, "A review on the current applications of artificial intelligence in the operating room," *Surgical Innovation*, vol. 28, pp. 611–619, 2021.

[9] I. J. Gerard, M. Kersten-Oertel, et al., "Brain shift in neuronavigation of brain tumors: A review," *Medical Image Analysis*, vol. 35, pp. 403–420, 2017.

[10] S. T. Solís, C. de Quintana Schmidt, et al., "Intraoperative imaging in the neurosurgery operating theatre: A review of the most commonly used techniques for brain tumour surgery," *Neurocirugía (English Edition)*, vol. 31, pp. 184–194, 2020.

[11] R. U. Gandhe and C. P. Bhave, "Intraoperative magnetic resonance imaging for neurosurgery – an anaesthesiologist's challenge," *Indian Journal of Anaesthesia*, vol. 62, pp. 411, 2018.

[12] I. J. Gerard, M. Kersten-Oertel, et al., "Brain shift in neuronavigation of brain tumors: An updated review of intra-operative ultrasound applications," *Frontiers in Oncology*, vol. 10, pp. 618837, 2021.

[13] D. C. A. Bastos, P. Juvekar, et al., "Challenges and opportunities of intraoperative 3D ultrasound with neuronavigation in relation to intraoperative MRI," *Frontiers in Oncology*, vol. 11, pp. 656519, 2021.

[14] J. T. Senders, I. S. Muskens, et al., "Agents for fluorescence-guided glioma surgery: a systematic review of preclinical and clinical results," *Acta Neurochirurgica*, vol. 159, pp. 151–167, 2016.

[15] R. Sun, H. Cuthbert, and C. Watts, "Fluorescence-guided surgery in the surgical treatment of gliomas: Past, present and future," *Cancers*, vol. 13, pp. 3508, 2021.

[16] H. Fabelo, R. Leon, et al., "3D decision support tool for brain tumour surgery: The STRATUM project," *27th Euromicro Conference on Digital System Design (DSD)*, pp. 443–450, 2024.

[17] F. Manni, F. V. D. Sommen, et al., "Hyperspectral imaging for glioblastoma surgery: Improving tumor identification using a deep spectral-spatial approach," *Sensors*, vol. 20, pp. 6955, 2020.

[18] G. Urbanos, A. Martín, et al., "Supervised machine learning methods and hyperspectral imaging techniques jointly applied for brain cancer classification," *Sensors*, vol. 21, pp. 3827, 2021.

[19] N. Baig, H. Fabelo, et al., "Empirical mode decomposition based hyperspectral data analysis for brain tumor classification," *43rd Annual International Conference of IEEE Engineering in Medicine & Biology Society (EMBC)*, pp. 2274–2277, 2021.

[20] H. Fabelo, M. Halicek, et al., "Deep learning-based framework for in vivo identification of glioblastoma tumor using hyperspectral images of human brain," *Sensors*, vol. 19, pp. 920, 2019.

[21] R. Leon, H. Fabelo, et al., "Hyperspectral imaging benchmark based on machine learning for intraoperative brain tumour detection," *npj Precision Oncology*, vol. 7, pp. 1–17, 2023.

[22] H. Mangotra, S. Srivastava, et al., "Hyperspectral imaging for early diagnosis of diseases: a review," *Expert Systems*, vol. 40, no. 8, pp. e13311, 2023.

[23] I.-C. Wu, Y.-C. Chen, et al., "Advancements in hyperspectral imaging and computer-aided diagnostic methods for the enhanced detection and diagnosis of head and neck cancer," *Biomedicines*, vol. 12, no. 10, 2024.

[24] M. Halicek, H. Fabelo, et al., "In-vivo and ex-vivo tissue analysis through hyperspectral imaging techniques: Revealing the invisible features of cancer," *Cancers*, vol. 11, 2019.

[25] M. A. Calin, A. C. Calin, and D. N. Nicolae, "Application of airborne and spaceborne hyperspectral imaging techniques for atmospheric research: past, present, and future," *Applied Spectroscopy Reviews*, vol. 56, pp. 289–323, 2021.

[26] B. Lu, P. D. Dao, et al., "Recent advances of hyperspectral imaging technology and applications in agriculture," *Remote Sensing*, vol. 12, pp. 2659, 2020.

[27] T. Adão, J. Hruška, et al., "Hyperspectral imaging: A review on UAV-based sensors, data processing and applications for agriculture and forestry," *Remote Sensing*, vol. 9, pp. 1110, 2017.

[28] Y. Z. Feng and D. W. Sun, "Application of hyperspectral imaging in food safety inspection and control: A review," *Critical Reviews in Food Science and Nutrition*, vol. 52, pp. 1039–1058, 2012.

[29] M. Ángeles Fernández de la Ossa, J. M. Amigo, and C. García-Ruiz, "Detection of residues from explosive manipulation by near infrared hyperspectral imaging: A promising forensic tool," *Forensic Science International*, vol. 242, pp. 228–235, 2014.

[30] G. J. Edelman, E. Gaston, et al., "Hyperspectral imaging for non-contact analysis of forensic traces," *Forensic Science International*, vol. 223, pp. 28–39, 2012.

[31] M. Shimoni, R. Haelterman, and C. Perneel, "Hypersectral imaging for military and security applications: Combining myriad processing and sensing techniques," *IEEE Geoscience and Remote Sensing Magazine*, vol. 7, pp. 101–117, June 2019.

[32] S. Puustinen, H. Vrzáková, et al., "Hyperspectral imaging in brain tumor surgery—evidence of machine learning-based performance," *World Neurosurgery*, vol. 175, pp. e614–e635, 2023.

[33] R. Mühle, H. Ernst, et al., "Workflow and hardware for intraoperative hyperspectral data acquisition in neurosurgery," *Biomedizinische Technik. Biomedical engineering*, vol. 66, pp. 31–42, 2020.

[34] R. Vandebriel, S. Luthman, et al., "Integrating hyperspectral imaging in an existing intra-operative environment for detection of intrinsic brain tumors," *SPIE*, vol. 12368, pp. 65–74, 2023.

[35] T. Giannantonio, A. Alperovich, et al., "Intra-operative brain tumor detection with deep learning-optimized hyperspectral imaging," *SPIE*, vol. 12373, pp. 80–98, 2023.

[36] S. K. Roy, G. Krishna, et al., "HybridSN: Exploring 3D-2D CNN feature hierarchy for hyperspectral image classification," *IEEE Geoscience and Remote Sensing Letters*, vol. 17, pp. 277–281, 2020.

[37] J. He, L. Zhao, et al., "HSI-BERT: Hyperspectral image classification using the bidirectional encoder representation from transformers," *IEEE Transactions on Geoscience and Remote Sensing*, vol. 58, pp. 165–178, 2020.

[38] L. Sun, G. Zhao, et al., "Spectral-spatial feature tokenization transformer for hyperspectral image classification," *IEEE Transactions on Geoscience and Remote Sensing*, vol. 60, 2022.

[39] B. Liu, A. Yu, et al., "DSS-TRM: deep spatial–spectral transformer for hyperspectral image classification," *European Journal of Remote Sensing*, vol. 55, pp. 103–114, 2022.

[40] Z. Zhao, D. Hu, et al., "Convolutional transformer network for hyperspectral image classification," *IEEE Geoscience and Remote Sensing Letters*, vol. 19, 2022.

[41] G. Lu and B. Fei, "Medical hyperspectral imaging: a review," *Journal of Biomedical Optics*, vol. 19, pp. 10901, 2014.

[42] B. Martinez, R. Leon, et al., "Most relevant spectral bands identification for brain cancer detection using hyperspectral imaging," *Sensors*, vol. 19, pp. 5481, 2019.

[43] I. Guyon, J. Weston, et al., "Gene selection for cancer classification using support vector machines," *Machine Learning*, vol. 46, pp. 389–422, 2002.

[44] J. Gao, Q. Du, et al., "Ant colony optimization for supervised and unsupervised hyperspectral band selection," *Workshop on Hyperspectral Image and Signal Processing, Evolution in Remote Sensing*, pp. 1–4, 2013.

[45] A. Dosovitskiy, L. Beyer, et al., "An image is worth 16x16 words: Transformers for image recognition at scale," *ICLR - 9th International Conference on Learning Representations*, 2020.

[46] H. Fabelo, S. Ortega, et al., "In-vivo hyperspectral human brain image database for brain cancer detection," *IEEE Access*, vol. 7, pp. 39098–39116, 2019.